CONF-810415--7

DEVELOPMENTS IN TOKAMAK TRANSPORT MODELING*

W. A. Houlberg, S. E. Attenberger, and L. L. Lao
Oak Ridge National Laboratory
Oak Ridge, Tennessee

A variety of numerical methods for solving the time-dependent fluid transport equations for tokamak plasmas is presented. Among the problems discussed are techniques for solving the sometimes very stiff parabolic equations for particle and energy flow, treating convection-dominated energy transport that leads to large cell Reynolds numbers, optimizing the flow of a code to reduce the time spent updating the particle and energy source terms, coupling the one-dimensional (1-D) flux-surface-averaged fluid transport equations to solutions of the 2-D Grad-Shafranov equation for the plasma geometry, handling extremely fast transient problems such as internal MHD disruptions and pellet injection, and processing the output to summarize the physics parameters over the potential operating regime for reactors. Emphasis is placed on computational efficiency in both computer time and storage requirements.

*Research sponsored by the Office of Fusion Energy, U. S. Department of Energy, under contract W-7405-eng-26 with the Union Carbide Corporation.

MGW

DEVELOPMENTS IN TOKAMAK TRANSPORT MODELING

INTRODUCTION

Efforts to model the time- and spatial-dependent behavior of tokamak plasmas have grown over the past decade from a few small codes containing simplified treatments of the particle and energy sources and losses to a large number of sophisticated codes that provide an ever increasing impact on our interpretation and prediction of the behavior of tokamak plasmas. The increased sophistication has been made possible not only by our improved understanding of the physical processes but also by the advances made in numerical methods for solving the complicated sets of highly nonlinear equations. All of the actively used codes are being improved continuously by changing the physics, computational techniques, and flow. Because of this, "user's manuals" and "standard" techniques are essentially nonexistent. Therefore, it would be a monumental undertaking to review all the variations in physical approximations and numerical techniques of tokamak transport codes. In this paper we will concentrate on the WHIST code which has many features similar to those of other transport codes; indeed, many of the concepts and methods have been borrowed from other codes. WHIST is a 1-1/2-dimensional (1-1/2-D) (1-D transport plus 2-D MHD equilibrium), time-dependent transport code.

In the following two sections, we devote most of our discussion to the basic 1-D, time-dependent transport equations and the 2-D MHD equilibrium equations and methods for solving them. Transient physics phenomena associated with internal MHD instabilities and pellet injection are discussed in the next section. A new approach to using time-dependent transport codes for reactor studies is then introduced. Finally, we close with a view of where significant new advances in physics and numerical techniques will have to be made.

SOLVING THE TRANSPORT EQUATIONS

THE TRANSPORT EQUATIONS IN FLUX COORDINATES

The tokamak plasma has a toroidal geometry and in some cases a noncircular cross section in the smaller dimension that makes rigorous mathematical analysis impossible. There are, however, a few simplifying assumptions that can reduce the transport equations to cylindrical form, with toroidicity and noncircularity entering through transport coefficients and geometric factors. In the limit of low toroidal field ripple, the plasma is uniform in the toroidal direction (axisymmetric) because of the very fast toroidal transit times of the ionized particles. There is also a poloidal component to the magnetic field produced by a current driven in the toroidal direction. The plasma safety factor q, which is typically of the order of 1-5 across the plasma, is the number of transits a magnetic field line makes in the toroidal direction per transit in the poloidal direction. Because particle orbits basically follow the magnetic field lines, the time scale for flow in the poloidal direction is nearly as fast as in the toroidal

direction. In the absence of magnetic islands or ergodicity, the field lines then trace out a set of nested magnetic flux surfaces with plasma densities and energies constant on a flux surface. A set of flux-surface-averaged equations can then be derived to follow the flow of particles, energy, and current diffusion on the much slower time scale of transport between flux surfaces.[1,2] The resulting fluid equations for particles and energy are given by

$$\frac{\partial}{\partial t}(V' n_j) = -(V' \Gamma_j)' + V' S_{pj} - V' \frac{\Gamma_{\parallel j}}{L_\parallel} \tag{1}$$

for each of the thermal ion densities n_j, and the electrons are subject to charge neutrality constraints

$$n_e = \sum_j z_j n_j + \sum_j z_j n_{jf} + z_{im} n_{im} \ , \tag{2}$$

$$\tilde{\Gamma}_e = \sum_j z_j \Gamma_j \ , \text{ and} \tag{3}$$

$$\tilde{\Gamma}_{\parallel e} = \sum_j z_j \Gamma_{\parallel j} \ . \tag{4}$$

The energy balance equations are

$$\frac{3}{2}\frac{\partial}{\partial t}\sum_j \left[(V')^{5/3} n_j T_i\right] = \sum_j \left\{-(V')^{2/3}(V' \tilde{Q}_j + \frac{5}{2} V' T_i \Gamma_j)' + (V')^{5/3}\left[\frac{\tilde{\Gamma}_e}{n_e}(n_j T_i)' + Q_{ej} + Q_{Ej} - \frac{\tilde{Q}_{\parallel j}}{L_\parallel}\right]\right\} \tag{5}$$

for the thermal ion components, which are assumed to have a common Maxwellian temperature T_i, and

$$\frac{3}{2}\frac{\partial}{\partial t}\left[(V')^{5/3} n_e T_e\right] = -(V')^{2/3}(V' \tilde{Q}_e + \frac{5}{2} V' T_e \Gamma_e)' + (V')^{5/3}\left[-\frac{\tilde{\Gamma}_e}{n_e}\left(\sum_j n_j T_i\right)' - \sum_j Q_{ej} + Q_{OH} + Q_{Ee} - \frac{\tilde{Q}_{\parallel e}}{L_\parallel}\right] \tag{6}$$

for the electron fluid with a Maxwellian temperature T_e. All terms in the above set of equations are functions of the effective radial coordinate ρ, with primes denoting differentiation with respect to ρ. V is the plasma volume contained within a flux surface; V' then represents an effective surface area. The particle fluxes for the ionic species $\tilde{\Gamma}_j$ are effective flux surface averaged such that $V'\tilde{\Gamma}_j$ represents the total number of ions flowing across the surface ρ per unit time. The conduction heat fluxes $\tilde{Q}_j$ and $\tilde{Q}_e$ similarly represent effective flux-surface-averaged quantities. The terms with the $\parallel$ subscripts denote losses of particles and energy along the field lines in the scrape-off layer, where field lines are intercepted by a

divertor or limiter. $L_{\parallel}$ is the effective parallel flow length to the divertor or limiter. Note that the parallel and radial flows are treated as being separately ambipolar (charge conserving) in equations 3 and 4. In reality, this approximation is likely not valid, but our lack of understanding of the transport processes in the scrape-off layer prevents more rigorous treatment. Q_{ej} is the flow of energy between electrons and ion specie j, usually called the rethermalization term, and Q_{OH} is the ohmic heating (OH) term. The third term on the right in equations 5 and 6 represents a transfer of energy from ions to electrons due to particles flowing down a pressure gradient. These flow-work terms are sometimes neglected or in part combined with the convective flow terms. The nonrigorous treatment of these terms is probably justifiable because classical collisional transport processes were used in ordering and relating terms in the derivation of the equations while in practice nonclassical processes dominate the transport. In equation 2 for the electron density, allowance has been made for electrons associated with fast-ion components (neutral beam ions and fusion products) and a stationary impurity component. We will not discuss these terms further in this paper; we only note that these components are generally treated as species separate from the thermal ions.

We have stated that ρ represents a label for a flux surface and that the flows of particles and energies in equations 1, 5, and 6 are relative to that flux surface. At any instant in time a flux surface may be labeled with either the toroidal or poloidal flux, but these fluxes diffuse with respect to each other during the evolution of the plasma. The choice of one or the other as a flux surface label is arbitrary and leads to differences in the treatment of the problem. The toroidal flux is relatively constant in real space (unless compression is considered) because it is dominated by the strong vacuum toroidal field. Weak paramagnetic effects are introduced by the toroidal current and diamagnetic effects by the plasma kinetic pressure. On the other hand, the poloidal flux generally changes more rapidly due to increasing toroidal current and subsequent resistive diffusion. In the WHIST transport code, we do not affix our ρ label to either the toroidal or poloidal flux but instead use the half-diameter of the plasma. This is a matter of convenience because we use a fixed-boundary calculation for the MHD equilibrium. Both the toroidal and poloidal magnetic fluxes diffuse with respect to the labeled surfaces.

The current diffusion equation can be cast in several forms. Generally, the poloidal magnetic field is used as the independent variable, and the toroidal current, current density, toroidal electric field, and plasma safety factor are treated as dependent variables. In this form Faraday's law is given by

$$\frac{\partial \tilde{B}_p}{\partial t} = (v_\phi \tilde{B}_p)' + \tilde{E}' \quad , \tag{7}$$

where v_ϕ represents the velocity of a surface of constant toroidal flux relative to the surface labeled ρ. This term is generally small with our choice of ρ. The toroidal component of the plasma current integrated from the magnetic axis out to surface ρ, $I(\rho)$, and the plasma safety factor q are related to $\tilde{B}_p$ through the plasma geometry:

$$\mu_o I = 2\pi R_o G_\theta \tilde{B}_p \quad , \tag{8}$$

$$q = G_\phi G_\theta \frac{F}{I} \quad , \tag{9}$$

$$G_\theta \equiv \langle g_{\theta\theta}/\sqrt{g} \rangle \quad , \text{ and} \tag{10}$$

$$G_\phi \equiv \langle \sqrt{g}/g_{\phi\phi} \rangle \quad , \tag{11}$$

where R_o is the geometric center of the plasma and G_θ and G_ϕ are dimensionless flux-surface-averaged geometric factors that will be discussed later. F is the poloidal current integrated from outside the plasma to surface ρ and is used to evaluate the toroidal flux:

$$F^2 = F_o^2 + \int_\rho^{a_o} \left(\frac{2P'V'}{\mu_o G_\phi} + \frac{(I^2)'}{G_\phi G_\theta} \right) d\rho \quad , \text{ where} \tag{12}$$

$$\mu_o F_o \equiv 2\pi R_o B_{To} \quad . \tag{13}$$

In equation 12 P is the total plasma kinetic pressure summed over all plasma components.

Using an Ohm's law that relates the components of the electric field and current density parallel to the total magnetic field and then flux surface averaging gives a relationship between the effective electric field $\tilde{E}$, the effective total current density $\tilde{J}$, and the effective non-ohmically-driven current density $\tilde{J}_s$:

$$\tilde{E} = \eta_\parallel (\tilde{J} - \tilde{J}_s) \quad , \tag{14}$$

where $\eta_\parallel$ is the electrical resistivity parallel to the total magnetic field.

Ampere's law is used to relate $\tilde{J}$ to I (and similarly $\tilde{J}_s$ to the current driven source I_s) in the form

$$\tilde{J} = \frac{F}{2\pi R_o G_\phi} \left(\frac{I}{F} \right)' \quad . \tag{15}$$

The effective current density $\tilde{J}$ cannot be used to evaluate the OH term in equation 6. An effective ohmic current density can be defined as

$$\tilde{J}_{OH} \equiv \frac{(2\pi R_o)^2}{\mu_o V'} (G_\theta \bar{B}_p)' = 2\pi R_o \frac{I'}{V'} \quad \text{so that} \tag{16}$$

$$Q_{OH} = \tilde{E}\tilde{J}_{OH} \quad . \tag{17}$$

All the effective quantities have been chosen so that they reduce to the usual definitions in low-beta, circular cross section plasmas where the geometric quantities become

$$V' \simeq 4\pi^2 R_o \rho \text{ and}$$

$$G_\theta \simeq G_\phi \simeq \frac{\rho}{R_o} \quad .$$

FINITE-DIFFERENCE METHODS FOR THE SPATIAL VARIATION

Equations 1, 5, 6, and 7 constitute the basic set of parabolic partial differential equations for tokamak transport. A cell method for obtaining a finite-differenced form of the transport equations can be set up on a nonuniform spatial grid in such a way that spatial derivatives are second order accurate and particle and energy conservation is ensured.[3] Let ρ_i represent a discrete number of points N in the plasma and construct a cell around each of these points. If the boundaries of the cells ρ_i^M are defined as being midway between the main grid points, the particle and energy fluxes become second order accurate:

$$\rho_i^M = \frac{\rho_i + \rho_{i-1}}{2} \quad \text{and}$$

$$\rho_1^M = \rho_1 = 0.$$

The last node on the main grid ρ_N is a dummy node that is used only for applying the outer-boundary condition so that the outer boundary of the last cell represents the edge of the plasma, $\rho_N^M = a_o$.

Integrate equation 1 over a cell to obtain the finite-differenced form:

$$\frac{\partial}{\partial t}\int_{\rho_i^M}^{\rho_{i+1}^M} n_j V' d\rho = -V'\Gamma_j\Big|_{\rho_i^M}^{\rho_{i+1}^M} + \int_{\rho_i^M}^{\rho_{i+1}^M} V' d\rho \left(S_{pj} - \frac{\tilde{\Gamma}_{\|j}}{L_\|}\right) . \tag{18}$$

Noting that V' integrated over the cell is just the cell volume, then the left-hand side of equation 18 is the rate of change of the total number of particles in the cell, the first term on the right is the flow of particles across the cell boundaries, and the last terms are cell-integrated sources and losses. If the volume of the cell is changing slowly in time, it can be taken outside the time derivative and the equation divided by the cell volume ΔV_i becomes

$$\frac{\partial n_{j,i}}{\partial t} = -\frac{V'_{i+1}\Gamma_{j,i+1} - V'_i\Gamma_{j,i}}{\Delta V_i} + S_{pj,i} - \frac{\tilde{\Gamma}_{\|j,i}}{L_{\|i}} \quad , \tag{19}$$

where the density and source and loss terms are interpreted as being appropriate cell averages. The effective surface areas V'_i and the particle fluxes $\tilde{\Gamma}_{j,i}$ are to be defined at the cell interfaces ρ_i^M. The parallel loss

term is nonzero only in the scrape-off layer near the plasma edge. A fine mesh is required there because of the sharper gradients and atomic physics processes. The mesh is set up so that the limiter tip or separatrix lies at an interface and cells lie entirely in the plasma or scrape-off region. The radial flux can be divided into two terms, one due to diffusion on the density gradient of specie j (the dominant or "diagonal" term) and the remainder due to temperature gradients, electric fields, etc:

$$\tilde{\Gamma}_j = -D_j \langle |\nabla\rho|^2 \rangle_f \frac{\partial n_j}{\partial \rho} + \Gamma^o_j \quad , \tag{20}$$

where the gradient metric $\langle |\nabla\rho|^2 \rangle_f$ represents the flux-surface-averaged conversion factor from gradients in ρ to gradients in real space. In finite-differenced form, equation 20 becomes

$$\tilde{\Gamma}_{j,i} = -D_{j,i} \langle |\nabla\rho|^2 \rangle_{fi} \frac{n_{j,i} - n_{j,i-1}}{\rho_i - \rho_{i-1}} + \Gamma^o{}_{j,i} \quad . \tag{21}$$

The diffusion coefficient and gradient metric are evaluated on the interface grid, and the gradient is central differenced because the interface lies midway between the density grid points.

Equations 5 and 6 can be differenced in the same way but must first be divided by $(V')^{2/3}$. The energy fluxes $\tilde{Q}_j$ and $\tilde{Q}_e$ are treated similar to the way the particle flux is differenced in equation 21 except that the diagonal terms are for T_i and T_e gradients, respectively. In treating empirical transport models, the factor 3/2 is used instead of 5/2 in the convective terms of equations 5 and 6 and the flow-work terms are neglected.

The finite-differenced form for the current diffusion equation is obtained by first integrating Ampere's equation (equation 15) over a cell then substituting into Faraday's equation (equation 7):

$$\int_{\rho_i^M}^{\rho_{i+1}^M} \frac{\tilde{J} G_\phi}{F} \, d\rho = \frac{1}{2\pi R_o} \frac{I}{F} \Bigg|_{\rho_i^M}^{\rho_{i+1}^M} \quad . \tag{22}$$

Because $G_\phi \sim \rho$, we can take a factor of $G_\phi/\rho F$ outside the integral on the left as a weakly varying term and interpret the resulting $\tilde{J}$ as an effective average current density in the cell:

$$\tilde{J}_i \frac{\left(\rho_{i+1}^M\right)^2 - \left(\rho_i^M\right)^2}{2} \frac{1}{2}\left(\frac{G_{\phi i+1}}{\rho_{i+1}^M F_{i+1}} + \frac{G_{\phi i}}{\rho_i^M F_i}\right) = \frac{1}{2\pi R_o}\left(\frac{I_{i+1}}{F_{i+1}} - \frac{I_i}{F_i}\right) . \tag{23}$$

At the magnetic axis, $I_1 = \rho_1^M = G_{\phi 1} = 0$, so the expression for J_1 becomes

$$\tilde{J}_1 = \frac{1}{2\pi R_o}\frac{2I_2}{\rho_2^M G_{\phi 2}} \quad . \tag{24}$$

The integrated toroidal and poloidal currents I and F and the metric G_ϕ are defined at the cell interfaces, and $\tilde{J}$ is defined on the ρ_i grid. In equation 14 $\tilde{E}$, $\tilde{J}_s$, and $\eta_\parallel$ are also defined on the ρ_i grid. For convenience, we will define an effective cross-sectional area ΔA_i for each cell to simplify the notation in equation 23:

$$\Delta A_i \equiv 2\pi R_o F_o \frac{\left(\rho_{i+1}^M\right)^2 - \left(\rho_i^M\right)^2}{2}\frac{1}{2}\left(\frac{G_{\phi i+1}}{\rho_{i+1}^M F_{i+1}} + \frac{G_{\phi i}}{\rho_i^M F_i}\right),$$

$$\Delta A_1 \equiv 2\pi R_o F_o \frac{\rho_2^M G_{\phi 2}}{2F_2} \quad ; \text{ then}$$

$$\Delta A_i \mathcal{J}_i = F_o\left(\frac{I_{i+1}}{F_{i+1}} - \frac{I_i}{F_i}\right) \quad . \tag{25}$$

Using equations 8, 14, and 25, the finite-differenced form for equation 7 becomes

$$\frac{\partial \tilde{B}_{pi}}{\partial t} = \frac{v_{\phi i+1}\tilde{B}_{pi+1} - v_{\phi i-1}\tilde{B}_{pi-1}}{\rho_{i+1}^M - \rho_{i-1}^M} - \frac{\left(\eta_{\parallel i}\mathcal{J}_{Si} - \eta_{\parallel i-1}\mathcal{J}_{Si-1}\right)}{\rho_i - \rho_{i-1}}$$

$$+ \frac{2\pi R_o F_o}{\mu_o(\rho_i - \rho_{i-1})}\left[\frac{\eta_{\parallel i}}{\Delta A_{i-1}}\left(\frac{G_{\theta i+1}\tilde{B}_{pi+1}}{F_{i+1}} - \frac{G_{\theta i}\tilde{B}_{pi}}{F_i}\right)\right.$$

$$\left. - \frac{\eta_{\parallel i-1}}{\Delta A_{i-1}}\left(\frac{G_{\theta i}\tilde{B}_{pi}}{F_i} - \frac{G_{\theta i-1}\tilde{B}_{pi-1}}{F_{i-1}}\right)\right] \quad . \tag{26}$$

BOUNDARY CONDITIONS

The boundary conditions on the particle and energy balance equations are that the fluxes vanish at $\rho = 0$ and a condition at the plasma boundary that can take one of several forms. Vanishing particle flux at the boundary, $\Gamma_{j,N} = 0$, can be used to simulate full recycle or test particle conservation, but normally one of the following conditions is imposed:

$$n_{j,N} = n_j(a_o) \quad \text{or} \quad \frac{1}{n_j}\frac{\partial n_j}{\partial \rho}\bigg|_{a_o} = \frac{1}{\Delta_{nj}} \quad .$$

In finite-differenced form the gradient condition becomes

$$\frac{n_{j,N} - n_{j,N-1}}{\rho_N - \rho_{N-1}} = \frac{n_{j,N} + n_{j,N-1}}{2\Delta_{nj}} \quad ,$$

with similar options provided for the temperatures.

The boundary condition at the origin on $\tilde{B}_p$ is that $\tilde{B}_{p1} = 0$. The condition at the edge can correspond to either fixed total plasma current, fixed safety factor, or no applied electric field, which become, in finite-differenced form,

$$\tilde{B}_{pN} = \frac{\mu_o I_N}{2\pi R_o G_{\theta N}} \quad ,$$

$$\tilde{B}_{pN} = \frac{\mu_o F_N C_{\phi N}}{2\pi R_o q(a_o)} \quad , \text{ and}$$

$$\frac{G_{\theta N}\tilde{B}_{pN}}{F_N} = \frac{G_{\theta N-1}\tilde{B}_{pN-1}}{F_{N-1}} + \mu_o \mathcal{J}_{SN-1} \quad ,$$

respectively. The last condition comes from setting $\tilde{E}_{N-1} = 0$ and would result in current decay during a shutdown simulation. Note that the finite-differenced forms above have been constructed so that $\tilde{E}$ = constant (no radial dependence) in steady state.

WIGGLES IN THE RADIAL PROFILES

With some transport models, "wiggles" have been observed in the solution for the ion temperature profile near the outer boundary, as shown in Figure 1. These wiggles are time independent, so they are not associated with iterative or nonlinear effects. It is a classic case of large cell Reynolds numbers. The cell Reynolds number is calculated from the local flow velocity v_c, the cell mesh size $\Delta\rho$, and the local thermal conduction coefficient for the diagonal contribution to the heat flux:

$$R_c \equiv \frac{2V_c \Delta\rho}{\chi} \quad , \text{ where}$$

$$v_c \equiv \frac{(3/2\Gamma_T + \tilde{Q}^o)}{nT} \quad \text{and}$$

$$\tilde{Q} = -n\chi \frac{\partial T}{\partial \rho} + \tilde{Q}^o \quad .$$

Roache[4] shows that these spatial oscillations or wiggles can occur if R_c is large enough even in elementary linear problems with constant coefficients. In slab geometry the condition for the onset of wiggles is $R_c > 2$. When this happens, convection dominates the heat flow and the equation looks first order in its spatial variation. In the limit $v_c \to \infty$, the temperature solution should be flat. The outer-boundary condition essentially over-

specifies the equation, and a shocklike solution is superimposed on the temperature profile.

Figure 1 illustrates a case in which $R_c >> 2$ over the outer part of the plasma in the ion energy equation. As the spatial mesh size is decreased or the scale length for the gradient boundary condition is increased, the magnitude of the wiggle decreases, as shown in Figures 1(a) and (b), respectively. Under most circumstances, changing the mesh size and/or outer-boundary condition can reduce or eliminate the wiggles. However, there are cases, such as the one shown in Figure 1(c), where wiggles occur in an internal region. Here the convective and conductive heat flow are assumed to be comparable in the scrape-off region. In the confined plasma region, there is a sharp change in the transport model to one dominated by convection. We have used an upwind difference at the last cell in the main plasma when $R_c > 2$ to eliminate the wiggles, but this is equivalent to introducing an artificially enhanced thermal conductivity.[4] The upwind difference for the convection term in the boundary cell is given by

$$\tilde{\Gamma}_T \Big|_{\rho_i^M}^{\rho_{i+1}^M} = (1 - \Theta_c)\Gamma_{i+1} T_{i+1/2} - (1 + \Theta_c)\Gamma_i T_{i-1/2} \quad ,$$

where $\Theta_c \equiv \Theta(R_c - 2)$ is a Heaviside step function. Θ_c can be replaced with any function that turns on in the vicinity of $R_c = 2$ and obeys the condition $0 \leq \Theta_c \leq 1$. We have tried several other approaches including a modification of Lax's method but have not found any (other than decreasing the mesh size) that solve the problem without changing it. It should be noted that in multispecies plasmas, wiggles can occur if a main driving term for one of the profile fluxes is a density gradient of another specie. Criteria analogous to those used in defining R_c and v_c can be determined for mesh size limitations for a given set of plasma parameters.

FINITE-DIFFERENCE METHODS FOR THE TEMPORAL VARIATION

Each term in the particle and energy balance equations is expanded in time about $t + \theta\Delta t$. If all terms were time centered ($\theta = 0.5$), this would be a Crank-Nicholson method. Many transport codes have gone to more implicit methods to enhance the numerical stability, either using θ as a variable parameter or setting $\theta = 1$. Although the numerical stability improves if all terms are expanded about $\theta > 0.5$,[3] the critical terms that govern the numerical stability are the diagonal contributions to the fluxes and the parallel loss terms in the scrape-off layer.

Many of the terms in the transport equations are highly nonlinear and not worth the effort to linearize for implicit time treatment. Expressions for the transport coefficients and various particle and energy source and loss terms fall in this category. If accuracy is important for the time expansion, then these terms can be evaluated explicitly at predicted values for the parameters.[3] A corrector loop can also be added, as in the PROCTR[5] or BALDUR codes,[6] which not only provides a check on the convergence of the solution at each timestep but generally improves numerical stability. A schematic flow diagram for the WHIST code is shown in Figure 2, in which a corrector loop has been added for the purpose of illustration, although the

code does not currently contain a corrector loop. The predictor-corrector method shown in Figure 2 has the advantage of being able to run without the corrector loop if either $N_c = 0$ or the convergence criterion is not very stringent. Howe[5] has found the predictor-corrector loop advantageous for obtaining particle conservation when coupling solutions for particle transport in the plasma with recycle from the chamber walls.

FREQUENCY OF UPDATING MAJOR PHYSICS ROUTINES

There are a number of major parts of the physics calculations that are very time consuming and therefore not likely to be re-evaluated at each timestep. Among these are neutral beam heating terms, ionization and charge exchange profiles from gas puffing and wall recycle, and MHD equilibrium as noted in Figure 2. The calculations for particle and energy source terms are typically broken up into shape factors that are tied to fractional changes in the local or global density and/or temperature profiles and plasma geometry. Efforts have concentrated on including more physics in these terms while increasing the speed of computation, although these two goals are many times incompatible.

Computationally efficient yet accurate methods have been found for a number of the physics problems, although the ranges of validity may be restricted. Examples include SPUDNUT,[7] a slab model for neutral gas transport in large plasmas, which has been benchmarked against ANISN calculations; a semiempirical model for neutral beam deposition in noncircular plasmas;[8] velocity moments of the Fokker-Planck equation for calculating the thermalization of fast ions;[9] and a moments method of solving the Grad-Shafranov equation for MHD equilibrium that will be discussed in the next section of this paper.

Neutral beam deposition calculations for finite-sized beams injected into a plasma with noncircular, nonconcentric flux surfaces are a problem that has been treated rigorously only with relatively time-consuming Monte Carlo methods.[10] However, an approximate solution can be obtained by first calculating numerically the attenuation along a single ray representing the centerline of the beam and then constructing an algorithm that removes the singularity where the ray passes through the magnetic axis. The deposition profile in the center region can be approximated as a cubic in ρ and then matched onto the ray solution at some intermediate radius ρ_M. If ρ_M is taken as twice the finite beam radius, excellent agreement can be obtained between the two methods over a wide range of parameters.[8] A typical set of benchmark cases is shown in Figure 3. Computation times on the CDC 7600 are 8.5 ms for a deposition profile with the semiempirical method and 0.1 ms per particle for the Monte Carlo method.

MHD EQUILIBRIUM SOLUTIONS

THE GRAD-SHAFRANOV EQUATION

On the slow diffusion time scale of interest, the inertia term in the momentum balance equation can be neglected. For a 2-D axisymmetric toroidal system, substitution of this equation into Ampere's law yields the Grad-Shafranov equation

$$\Delta^* \psi(R,Z) = -\frac{8\pi^2 R}{c} J_\phi \quad , \tag{27}$$

where J_ϕ is the toroidal component of the current density

$$J_\phi = 2\pi cR\left[P'(\psi) + \frac{FF'(\psi)}{\pi c^2 R^2}\right], \tag{28}$$

ψ and F are the poloidal magnetic flux and the poloidal current enclosed between the axis of symmetry and the magnetic surface of interest, respectively, and

$$\Delta^* \psi(R,Z) = \frac{\partial^2 \psi}{\partial R^2} - \frac{1}{R}\frac{\partial \psi}{\partial R} + \frac{\partial^2 \psi}{\partial Z^2} \quad . \tag{29}$$

The Grad-Shafranov equation imposes a constraint on the flux surface geometry. As the plasma evolves through a sequence of MHD equilibrium states, the flux surface shape must change in a way such that the Grad-Shafranov equation is satisfied.

VARIATIONAL MOMENTS SOLUTIONS

Repeatedly solving the 2-D Grad-Shafranov equation for the evolving flux surface geometry can significantly increase the computer time and storage requirements of a transport code. A computationally efficient method to find approximate solutions to the Grad-Shafranov equation has been developed.[11] The flux surface coordinates (R,Z) are expanded in Fourier series in a poloidal angle θ that increases by 2π the short way around the torus:

$$R(\rho,\theta) = R_o(\rho) - R_1(\rho)\cos\theta + \sum_{n=2}^{n_R} R_n(\rho)\cos n\theta \quad \text{and} \tag{30}$$

$$Z(\rho,\theta) = E(\rho) \sum_{n=1}^{n_R} R_n(\rho)\sin n\theta \quad , \tag{31}$$

where ρ is a flux surface label and the flux surfaces are assumed to have up-down symmetry $Z(\rho,\theta) = Z(\rho,-\theta)$. Also, the poloidal angle θ has been chosen such that $Z_n(\rho) = E(\rho)R_n(\rho)$. The amplitude functions $R_o(\rho)$, $R_1(\rho)$, and $E(\rho)$ describe the shift, the minor radius, and the ellipticity of the flux surfaces, respectively, and the amplitude $R_2(\rho)$ describes their triangularity. A few terms ($n \leq 3$) in the Fourier series are generally sufficient to describe many plasma equilibria, including those for high-beta, strongly D-shaped plasmas. Thus, the problem of finding 2-D MHD equilibria is reduced to that of solving a few ordinary differential

equations for the amplitude functions $R_n(\rho)$ and $E(\rho)$. The equations describing $R_n(\rho)$ and $E(\rho)$ can be conveniently obtained using a variational principle. They can be shown to be moments of the Grad-Shafranov equation with basis functions M_{Rn} and M_E,

$$\langle M_{Rn} \tilde{G} \rangle = 0 \quad \text{and} \tag{32}$$

$$\langle M_E \tilde{G} \rangle = 0 \quad , \tag{33}$$

where $\tilde{G}$ is the Grad-Shafranov equilibrium operator in (ρ,ϑ) coordinates:

$$\tilde{G} = \frac{I^2(\rho)}{\pi c^2 \sqrt{g}\, G_\vartheta} \left(\frac{\partial}{\partial \rho} \frac{g_{\vartheta\vartheta}}{\sqrt{g}\, G_\vartheta} - \frac{\partial}{\partial \vartheta} \frac{g_{\rho\vartheta}}{\sqrt{g}\, G_\vartheta} \right) + \frac{II'(\rho)}{\pi c^2 G_\vartheta} \left(\frac{g_{\vartheta\vartheta}}{g G_\vartheta} - \frac{1}{g_{\phi\phi} G_\phi} \right)$$

$$+ P'(\rho) \left(1 - \frac{\sqrt{g}}{g_{\phi\phi} G_\phi} \right) \quad . \tag{34}$$

The flux-surface-averaged quantities G_ϕ and G_ϑ are given by equations 10 and 11, respectively. The 3-D Jacobian of the transformation from (R,ϕ,Z) to (ρ,ϑ,ϕ) coordinates (ϕ is the ignorable coordinate) is given by

$$\sqrt{g} = R\tau \quad , \quad \text{where} \tag{35}$$

$$\tau = R_\vartheta Z_\rho - R_\rho Z_\vartheta \quad . \tag{36}$$

Here the subscripts ρ and ϑ on R and Z denote differentiation with respect to these variables. The elements of the metric tensor are

$$g_{\mu\nu} = R_\mu R_\nu + Z_\mu Z_\nu \qquad (\mu,\nu = \rho,\vartheta) \quad , \tag{37}$$

$$g_{\phi\phi} = R^2 \quad , \quad \text{and} \tag{38}$$

all other elements are zero. The basis functions are given by

$$M_{Ro} = RZ_\vartheta \quad , \tag{39}$$

$$M_{R1} = R(ER_\vartheta \sin\vartheta + Z_\vartheta \cos\vartheta) \quad , \tag{40}$$

$$M_{Rn} = R(ER_\vartheta \sin n\vartheta - Z_\vartheta \cos n\vartheta) \qquad (n > 2) \quad , \quad \text{and} \tag{41}$$

$$M_E = \sum_{n=1}^{n_R} R_n RR_\vartheta \sin n\vartheta \quad . \tag{42}$$

<A> is the poloidal-angle-averaging operator defined for any scalar A as

$$\langle A \rangle = \int_0^{2\pi} \frac{d\vartheta}{2\pi} A \quad .$$

COMPARISON WITH COMPLETE 2-D SOLUTIONS

The moments equations 32 and 33 form a set of coupled second-order ordinary differential equations. Given two driving functions $P(\rho)$ and $I(\rho)$, they are solved numerically with the boundary conditions corresponding to a fixed plasma boundary using a shooting technique.

In Figure 4 the flux surface contours (constant ρ contours) are shown for an ETF/INTOR equilibrium. The solid lines are from the moments calculation, and the dashed lines represent the calculation using a standard 2-D code. Figures 5(a)-5(c) illustrate the normalized shift $\tilde{S}(\rho)$, elongation $\tilde{E}(\rho)$, and triangularity $\tilde{D}(\rho)$ parameters of the flux surfaces for the exact 2-D and moments solutions. Figures 5(d)-5(f) provide a comparison of the effective surface area $V'(\rho)$, the safety factor $q(\rho)$, and the poloidal magnetic flux $\psi(\rho)$. The agreement between the moments method approximation and the 2-D results is well within acceptable limits for transport simulation, but the moments calculation is typically faster by a factor of 10 in computational speed and requires much less storage.

COUPLING TO THE TRANSPORT EQUATIONS

The 2-D equilibrium constraint is imposed on the 1-D transport equations as follows. An equilibrium calculation is performed using $P(\rho)$ and $I(\rho)$ to obtain the effective surface area $V'(\rho)$ and various geometric factors. The plasma density and temperatures are then readjusted adiabatically to be consistent with the new flux surface geometry using[2]

$$(n_j)_{new}(V')_{new} = (n_j)_{old}(V')_{old} \quad \text{and} \tag{43}$$

$$(T_j)_{new}(V')^{2/3}_{new} = (T_j)_{old}(V')^{2/3}_{old} \quad . \tag{44}$$

The toroidal current $I(\rho)$ is readjusted by keeping the safety factor q fixed (i.e., flux conserving):

$$\left(\frac{F}{I} G_\phi G_\vartheta\right)_{new} = \left(\frac{F}{I} G_\phi G_\vartheta\right)_{old} \quad . \tag{45}$$

All the above calculations and parameter readjustments occur in the box denoted MHD equilibrium in Figure 2. Next, transport calculations are carried out for one or more timesteps holding V' and the geometric factors

fixed, as shown in the main time loop of Figure 2, until certain physical parameters (densities, temperatures, magnetic field, etc.) have changed by a specified amount. Transport is halted, and the resulting $P(\rho)$ and $I(\rho)$ are used to calculate a new equilibrium.

TRANSIENT PHYSICS PROCESSES

Transient physics processes introduce a rapid change in the plasma parameters over a very short time scale; then the plasma relaxes over a longer transport time scale until the conditions are met for another plasma disturbance. Examples of the physical processes that exhibit this kind of behavior are pellet injection and some types of MHD instabilities such as sawtooth disruptions and double-tearing-mode disruptions for inverted current profiles. If the disturbances are frequent enough for pellet injection or sawtooth behavior, a continuous model can be constructed. The condition for a continuous model to be valid is that the repetition time for the disturbance be much less than the time scale for the relaxation of the profiles.

PELLET INJECTION

When a high-velocity pellet is injected into a large, hot reactor plasma, the pellet is expected to completely ablate in a period of a few hundred microseconds.[12] This time scale is much shorter than the 1-s time scale for radial flow but long compared to the time scale for electron energy flow along field lines. The rate of ablation of the pellet can then be calculated from the background plasma parameters using either an infinite- or finite-medium calculation.[13] All terms in equations 1, 5, and 6 are negligible on an ablation time scale except for the time derivatives on the left and the source and loss terms from pellet ablation on the right. These equations can be integrated over the ablation time interval to come up with conditions for step changes in the densities and temperatures due to injection of a pellet:

$$\int_{t_p-\varepsilon}^{t_p+\varepsilon} dt\left(\frac{\partial n_j}{\partial t} = S_{pj}\right) , \tag{46}$$

which gives the step condition

$$n_j(t_p + \varepsilon) = n_j(t_p - \varepsilon) + \Delta n_{pj} \quad . \tag{47}$$

Similarly, we find that the total electron and ion energy densities must be preserved with allowance made for a small amount of energy loss associated with the ablation and ionization of the pellet. Thus, to simulate discrete pellet injection, step changes are periodically made in the density and temperature profiles subject to particle and energy conservation restrictions on the short ablation time scale. The plasma transport simulation is then reinitiated with new profiles after the injection step.[14]

If the pellet repetition rate is rapid (i.e., short compared to both particle and energy transport time scales), then pellet injection can be simulated as a continuous process. The deposition profile is calculated

from the ablation profile, but the source term $\Delta n_{p,j}$ is averaged over the pellet repetition time to arrive at an effective average source strength. Typical reactor simulations with 20-ms repetition times for the pellets show good agreement between continuous and discrete pellet models because the transport time scales are of the order of 1 s.

INTERNAL MHD DISRUPTIONS

Detailed calculations for the conditions that lead to internal plasma disruptions and the redistribution of the plasma during disruption are extremely complex 2-D or 3-D nonlinear calculations involving both Alfven (microsecond) and transport (second) time scales.[15,16] Empirical models can, however, be constructed for transport modeling that preserve the gross features of the disruptions.

Using the flux surface parameters defined earlier, we can construct approximate helical flux functions for the sawtooth mode (m = 1, n = 1),

$$\chi_s^*(\rho) \simeq \int_o^\rho \left(\frac{1}{q} - 1\right) G_j \frac{\mu_o F}{2\pi R_o}\, d\rho' \quad ,$$

and double tearing mode,

$$\chi_{mn}^*(\rho) \simeq \int_{a_o}^\rho \left(\frac{n}{m} - \frac{1}{q}\right) G_j \frac{\mu_o F}{2\pi R_o}\, d\rho' \quad ,$$

where n and m denote the toroidal and poloidal mode numbers, respectively. These expressions are valid only in the circular cross section limit but have been extended into the noncircular regime using empirical arguments.

A condition or set of conditions must then be imposed on the q profile to determine when a disruption will occur. For the sawtooth disruption, this may be in the form of empirical conditions such as $q(o) < q_c < 1$ or $q(r_s) < 1$. The critical parameters q_c or r_s can be constants or can be determined self-consistently from the plasma profiles.[15] We have used $q_c \simeq 0.9$–0.92 to give generally good agreement with experimental results. In matching a given experiment, specification of the singular surface r_s is usually more direct. For the double tearing mode to occur, the safety factor must be double valued and rational, $q = m/n$. Usually we consider only n = 1 modes because these are likely to be the most unstable.

Next, the radial extent of the disruption r_o must be determined. In Kadomtsev's model[16] for the sawtooth disruption, the condition is given by $\chi_s^*(r_o) = 0$. For the double tearing mode, the condition is similar except that there are two rational q surfaces involved:

$$q(r_{s1}) = q(r_{s2}) = m/n \quad .$$

The extent of the double-tearing-mode disruption r_o is then determined from

$$\chi^*_{mn}(r_o) = \chi^*_{mn}(r_{s1}) \quad ,$$

where $r_{s1} < r_{s2} < r_o$.

The flux surfaces inside r_o must then be reconstructed. The simplest form for this reconstruction is to assume the new safety factor $q(\rho) = q(r_o)$ is uniform for $\rho < r_o$.

Because the flux surfaces reconnect during an internal disruption, the plasma density and temperature profiles are necessarily perturbed. Uniform redistribution of both density and energy has been used to successfully model the major features of experimental observations. Numerically, this is done with the constraints of particle and energy conservation over the region $\rho < r_o$. The transport and MHD evolution are then restarted with what is essentially a new set of initial conditions. The disruption appears as a step change in the profiles with appropriately preserved global conditions.

SCANNING THE PLASMA OPERATING REGIME

We have recently found a way to maximize the information gained from comprehensive transport simulations through the use of contour plots in density and temperature space. We would like to know how much supplementary heating power must be provided for the steady-state operation of a plasma at a given density and temperature, the corresponding plasma beta, and other parameters such as the fusion power output in a reactor. We can scan density and temperature space by providing feedback on the particle and energy sources and using time as a way to march from one equilibrium to the next. Figure 6 shows a set of beam power, fusion power, and beta contours for a typical tokamak reactor calculation. The results from eight time-dependent 1-1/2-D transport runs with the WHIST code were stacked to generate this set of plots. Each run is at a constant density maintained by feedback on the particle source. The temperature is slowly ramped from the initial state to the final temperature (20 keV in this case) by providing feedback on the neutral beam heating source. If the time scale for the ramp from initial to final temperatures is long compared to the time scale for the relaxation of the profiles, the plasma remains in near steady state. In Figure 6 the transport time scales are about 1 s whereas the simulation time for each constant density scan was 20 s. Comparison with 40-s simulations shows little difference. A set of data is generated along each scan that gives all source and loss rates from the plasma and major plasma parameters. This data set is then fed to a contour plotter. The set of eight transport sums to generate Figure 6 consumed about 10 min of CDC 7600 time and included the evolution of the MHD equilibria and the effects of the shift of the plasma at high beta on beam penetration and toroidal field ripple losses.

SUMMARY

The set of equations describing the evolution of tokamak plasmas possesses many features that present severe tests for computer analysis. Coupling the highly nonlinear 1-D equations for the density, temperature, and current profiles to the 2-D solution of the Grad-Shafranov equation for the changing geometry has many subtle difficulties. The debates over which methods are most appropriate or accurate are still continuing. Efforts at modeling

discontinuous processes such as pellet injection and MHD disruptions in plasma transport calculations have begun only during the past couple of years. These are areas where far greater effort will be concentrated in the future as we strive to gain further insight into disruptive processes in general and the plasma's ability to recover from disruptions. As more physics is incorporated into the models, the numerical techniques have to be made more efficient because both size and computation time can already approach the limits of many computer systems.

REFERENCES

1 F. L. Hinton and R. D. Hazeltine, Rev. Mod. Phys. 48 (1976), p 239.

2 J. T. Hogan, Nucl. Sci. Eng. 64 (1977), p 2.

3 W. A. Houlberg and R. W. Conn, Nucl. Sci. Eng. 64 (1977), p 141.

4 P. J. Roache, Computational Fluid Dynamics, Hermosa Publishers, Albuquerque, New Mexico (1972).

5 H. C. Howe (Oak Ridge National Laboratory), private communication, 1980; also to be published as "Hydrogen Recycle Modeling and Measurements in Tokamaks" in J. Nucl. Mat.

6 D. E. Post (Princeton Plasma Physics Laboratory), private communication, 1980.

7 K. A. Audenaerde, G. A. Emmert, and M. Gordinier, J. Comput. Phys. 34 (1980), p 268.

8 R. M. Wieland and W. A. Houlberg, "Neutral Beam Deposition in Large, Finite β, Noncircular Tokamak Plasmas," Oak Ridge National Laboratory Report ORNL/TM-7658 (1981).

9 J. D. Callen, R. J. Colchin, R. H. Fowler, D. G. McAlees, and J. A. Rome, Proc. Plasma Physics and Controlled Nuclear Fusion Research, Vol. 1, IAEA, Vienna (1974), p 645.

10 R. H. Fowler, J. A. Holmes, and J. A. Rome, "NFREYA-A Monte Carlo Beam Deposition Code for Noncircular Tokamak Plasmas," Oak Ridge National Laboratory Report ORNL/TM-6845 (1979).

11 L. L. Lao, S. P. Hirshman, and R. M. Wieland, "Variational Moment Solutions to the Grad-Shafranov Equation," Oak Ridge National Laboratory Report ORNL/TM-7616 (1981); submitted to Phys. Fluids.

12 S. L. Milora, J. Fusion Energy 1 (1981), p 15.

13 W. A. Houlberg, M. A. Iskra, H. C. Howe, and S. E. Attenberger, "Pellet-A Computer Routine for Modeling Pellet Fueling in Tokamak Plasmas," Oak Ridge National Laboratory Report ORNL/TM-6549 (1980).

14 W. A. Houlberg, H. C. Howe, and S. E. Attenberger, "Deuterium and Tritium Fueling in an ETF/INTOR Plasma with Divertor," Oak Ridge National Laboratory Report ORNL/TM-7124 (1980).

15 G. L. Jahns, M. Soler, B. V. Waddell, J. D. Callen, and H. R. Hicks, Nucl. Fusion 18 (1978), p 609.

16 B. Carreras, H. R. Hicks, and B. V. Waddell, Nucl. Fusion 19 (1979), p 583.

17 B. B. Kadomtsev, Sov. J. Plasma Phys. 1 (1975), p 389.

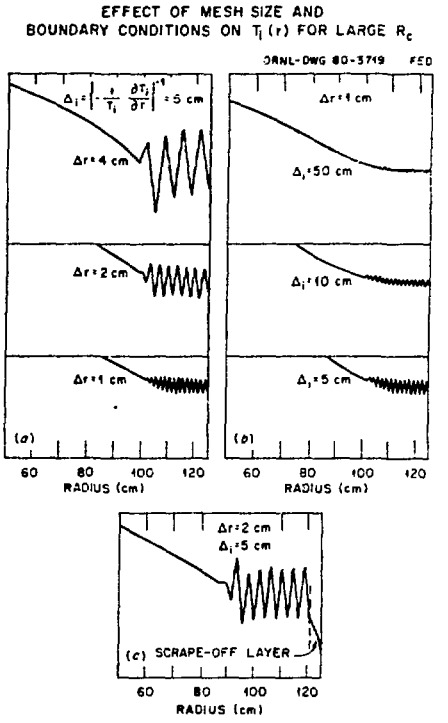

Figure 1. The Mesh Size (a), Boundary Conditions at the Wall (b), and Scrape-off Layer (c) Affect the Magnitude of Wiggles

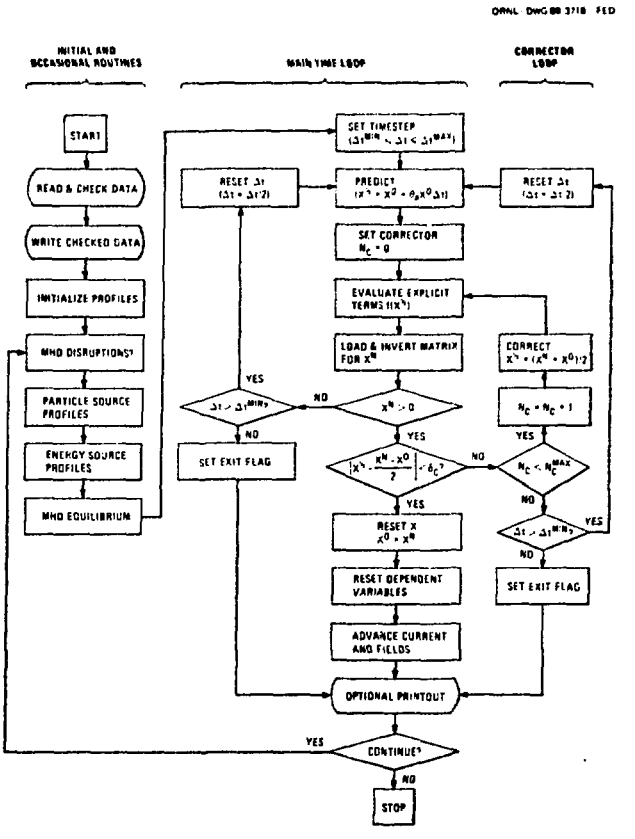

Figure 2. Flow Diagram for a Typical Plasma Transport Code

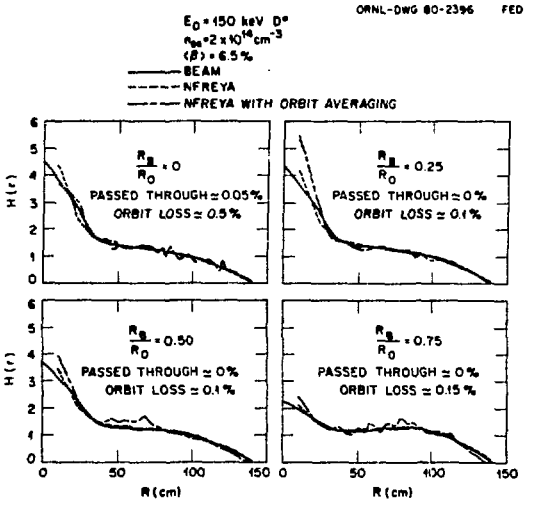

Figure 3. Comparison of Neutral Beam Deposition Profiles for BEAM (Analytical/Empirical) and NFREYA (Monte Carlo) Codes

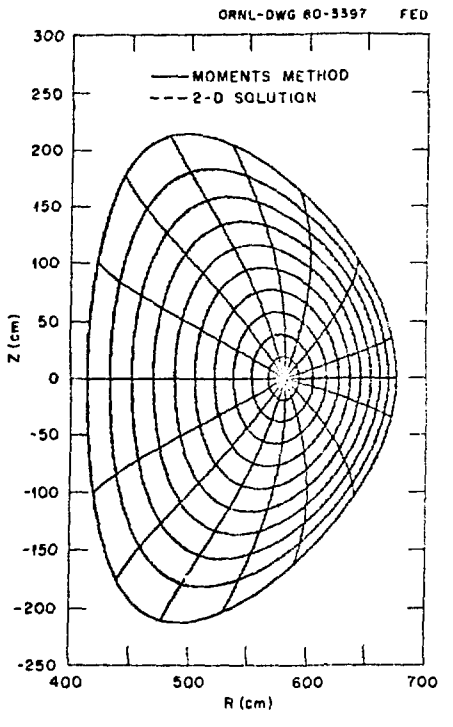

Figure 4. Comparison of Variational Moments and 2-D Solutions of Flux Surface Contours for a Typical Tokamak Equilibrium

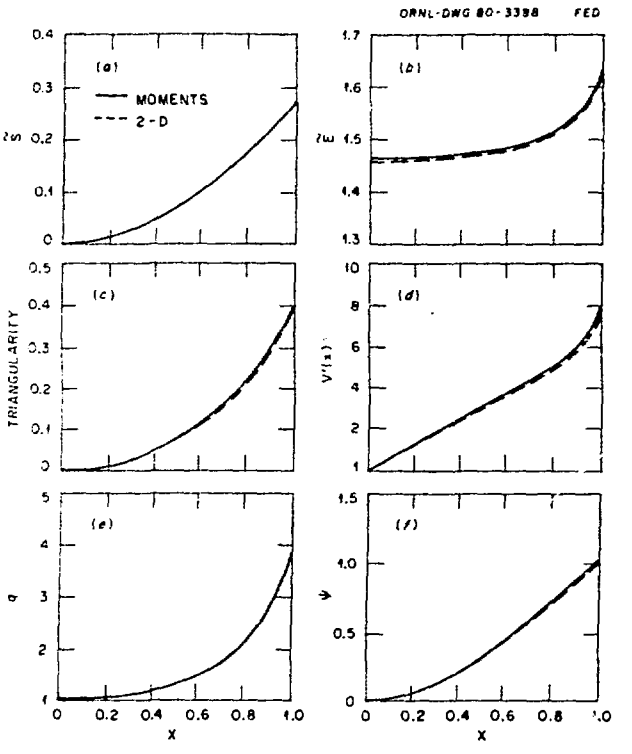

Figure 5. Comparison of Variational Moments and 2-D Solutions for the Geometric Quantities of the Equilibrium of Figure 4

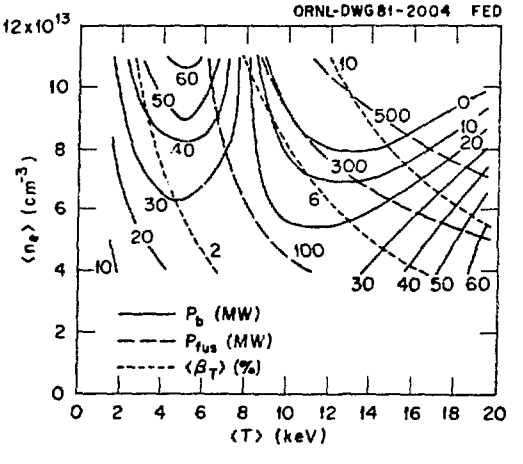

Figure 6. Plasma Operating Contours for a Typical Tokamak Reactor Simulation Generated with a 1-1/2-D Transport Code